Remote measurements of vertical profiles of atmospheric constituents with a UV–visible ranging spectrometer

K. Strong and R. L. Jones

A study of the feasibility of retrieving vertical profiles of atmospheric constituents with a new UV–visible ranging spectrometer recently described by R. L. Jones [*Optical Methods in Atmospheric Chemistry*, U. Platt and H. I. Schiff, eds., Proc. Soc. Photo-Opt. Instrum. Eng. **1715**, 393 (1992)] is presented. This instrument resembles a lidar, in that pulses of UV–visible radiation are transmitted vertically upward and backscattered to receiving optics. However, the pulse is a broadband source, and the receiving optics includes a two-dimensional CCD array that allows a series of absorption spectra to be recorded, each corresponding to a different altitude. This allows the simultaneous measurement of the vertical profiles of such atmospheric constituents as O_3, H_2O, and NO_2 in the troposphere and lower stratosphere. Formal retrieval theory has been used to model the retrieval of vertical profiles with this instrument, demonstrating that it should be possible to obtain profiles at accuracies better than 30% and resolution better than 3 km up to altitudes of 12–15 km. The way in which the measurement error, flash-lamp pulse length, CCD recording interval, and mixing-ratio profile each affect the accuracy and the vertical resolution of the retrieved profile has also been investigated.

Key words: Atmosphere, lidar, remote sensing, UV-visible spectroscopy, vertical profiles.

1. Introduction

The design of a new instrument that combines the techniques of UV–visible absorption spectroscopy[1] and lidar profiling[2,3] has recently been described by Jones.[4] This instrument is a ranging UV–visible spectrometer that will obtain vertically resolved measurements of backscattered radiation over an extended spectral region. This will allow the simultaneous determination of the vertical profiles of such species as O_3, H_2O, and NO_2, as well as aerosol and clouds, in the troposphere and lower stratosphere.

The ability to obtain spatial resolution along the line of sight is the major advantage of this measurement technique over current UV–visible absorption spectroscopy, as the latter provides only limited, if any, spatial resolution, particularly in the troposphere.[5,6] Although similar to the lidar technique in its vertical-resolving capability, the ranging instrument has the added advantage of recording absorptions over a wide spectral band, rather than at a pair of wavelengths relevant to a single absorber. It is therefore able to record the absorptions of several species simultaneously and to increase greatly the discrimination between constituents. In addition, the use of differential absorption analysis methods makes it possible to detect weaker absorbers ($\leq 0.1\%$ absorption) that are difficult to measure with the lidar technique.

In this paper the theoretical performance of the UV–visible ranging spectrometer is described, and the feasibility of using it to retrieve vertical profiles is assessed. Of particular interest is how various factors such as the number of retrieved profile points, the measurement noise, the width of the flash-lamp pulse, and the length of the CCD recording interval affect the accuracy and the vertical resolution of the retrieved profile.

2. Description of the Instrument

The principal components of the ranging instrument are a broadband pulsed xenon-arc lamp, transmitting and receiving telescopes, a grating spectrometer, and a two-dimensional CCD array detector. Short pulses

The authors are with the Cambridge Centre for Atmospheric Science, Department of Chemistry, University of Cambridge, Lensfield Road, Cambridge, CB2 1EW, United Kingdom. K. Strong is now with the Centre for Atmospheric Chemistry, York University, 4700 Keele Street, North York, Ontario, M3J 1P3, Canada.

Received 22 August 1994; revised manuscript received 18 April 1995.

0003-6935/95/276223-13$06.00/0.

of UV–visible radiation are transmitted vertically into the atmosphere in a beam of low divergence. This radiation is Rayleigh scattered at all altitudes, with a proportion being backscattered to the receiving optics and dispersed by the spectrometer onto the CCD detector. The range (or altitude) of the scattering can be determined from the time elapsed between transmission and reception, and the column abundance of a given species in the path can be deduced from its absorption spectrum. Measurements at discrete time intervals, which correspond to a series of altitudes, can thus be used to derive vertical profiles. This approach differs from the lidar technique in the use of a pulsed broadband light source and the method of recording return signals with the CCD detector array.

The combination of time resolution (hence range resolution) and spectral resolution, which is central to this instrument, is provided by the two-dimensional CCD array. In its usual mode of operation, a CCD is located in the image plane of a spectrometer, which disperses a spectrum across several rows of pixels. The incident photons are converted into charge, which is transferred from one pixel to the next in a given row, being swept column by column to the edge of the array for digitization. However, in the ranging instrument, the CCD is mounted at 90° to its conventional position, with only a few columns illuminated. Spectral discrimination is obtained by dispersing the spectrum across the pixels in a column, and time discrimination can now be obtained by shifting charge along the rows into the unilluminated region of the CCD array. The time resolution depends on the number of columns illuminated and on the time required for transfer of charge between columns. An additional advantage of the CCD detector is that charge can be shifted in both directions along a row, allowing the exposed columns to be returned to their original positions to record additional flash-lamp pulses. Thus a large number of pulses can be integrated on the CCD before readout to improve the signal to noise.

Calculations of the signal to noise and the detection limits anticipated for the ranging instrument have been performed by Jones.[4] The following system parameters were assumed: a 30-W arc lamp, which gave a uniform output from 200 to 1000 nm, with 15% of this output directed to within the 0.5-mrad acceptance angle of the collecting optics; a 400-mm-diameter collecting telescope; a grating efficiency of 0.5; a detector efficiency of 0.3; and an optical transmission of 0.6. The backscattered signal, in photons per nanometer per second, assuming Rayleigh scattering from 1-km vertical layers, was calculated for a range of altitudes. The results suggest that a signal-to-noise ratio of 1000, necessary for the detection of an absorption of 0.1%, will be achievable for ranges up to at least 11 km for certain combinations of integration time and wavelength range. For example, if a 30-nm wavelength interval were used for each constituent, information could be retrieved up to 7 km and 11 km by the use of integration times of 3 min and 20 min, respectively. Assuming that this 0.1% absorption can be resolved, the detection limits for a 1-km vertical path will be approximately 2 parts in 10^9 by volume (ppbv) for O_3, 150 parts in 10^6 by volume (ppmv) for H_2O, and 0.6 ppbv for NO_2. These will be sufficient for the detection of O_3 and H_2O, whose tropospheric mixing ratios are typically 10–100 ppbv and 5–10,000 ppmv but may require coarser vertical resolution for the detection of NO_2, whose tropospheric mixing ratio under clean conditions is typically 0.1–1 ppbv.

3. Simulating Measurements Made with the Ranging Spectrometer

In the study described below, formal retrieval theory is used to simulate and characterize the retrieval of vertical profiles with the ranging instrument. A number of methods for the inversion of geophysical data exist, some of a general nature and some having more limited applicability (see Twomey[7] for a general review and Rodgers[8] for a review emphasizing atmospheric applications). These can be divided into three categories: smoothing or regularization methods, statistical methods, and iterative methods.[9] Some of the first techniques to deal with the problem of determining the criteria that define the optimal retrieval consistent with a set of observations were the smoothing or regularization methods, developed independently by Twomey[10] and Tikhonov.[11] These have been applied to the analysis of conventional differential absorption lidar measurements[12] and used to generalize lidar theory to multiwavelength, multimaterial lidar.[13,14] In this paper, statistical methods have been used. In particular, the formulation of Rodgers[8,15] has been followed, as it is of general applicability and provides a particularly elegant method of combining *a priori* information with measurements and explicitly calculating the error on a retrieved profile from the errors in these quantities.

The retrieval and characterization of the system starts with the definition of a forward model F that relates a vector of m measurements, $\mathbf{y}$, to an atmospheric profile $\mathbf{x}$ defined at n levels:

$$\mathbf{y} = F(\mathbf{x}, \mathbf{b}) + \boldsymbol{\varepsilon}, \tag{1}$$

where $\mathbf{b}$ is a vector of model parameters and ε is the measurement error, assumed to be normally distributed about zero with error covariance $\mathbf{S}_y$. For a conventional two-wavelength differential absorption lidar, this forward model might be represented by the lidar equation, which can be written as[16,17]

$$P(Z, \lambda) = \frac{CE\beta(Z, \lambda)}{Z^2} \exp\left\{-2 \int_0^Z [\sigma(\lambda)N(z) + \alpha_{abs}(z, \lambda) + \alpha_{ext}(z, \lambda)]dz\right\}, \tag{2}$$

where $P(Z, \lambda)$ is the lidar return signal at range Z and wavelength λ, C is the system constant, E is the

energy of the laser pulse, $\beta(Z, \lambda)$ is the atmospheric backscattering coefficient, $\sigma(\lambda)$ is the absorption cross section of the gas of interest, $N(z)$ is the number density of the gas of interest, $\alpha_{abs}(z, \lambda)$ is the molecular absorption of all other gases, and $\alpha_{ext}(z, \lambda)$ is the extinction due to Rayleigh and Mie scattering. In this case, $P(Z, \lambda)$ would correspond to the measurements $\mathbf{y}$ and $N(z)$ would correspond to the profile $\mathbf{x}$, which is usually derived by applying the lidar equation at two wavelengths that are differentially absorbed by the species of interest.

However, in this study, a different approach has been taken. The signals recorded with the ranging instrument will be spectra of backscattered radiation dispersed over a significant spectral region, instead of being limited to a few discrete wavelengths. A set of measurements will therefore correspond to a series of spectra recorded at discrete time intervals. It is anticipated that these range-resolved measurements will be converted into vertical column abundances for more than one species by the use of the conventional analysis methods of UV–visible absorption spectroscopy.[18] Although the lidar equation has been generalized for multiwavelength, multimaterial applications by Warren,[13,14] and Zhao *et al.*[17,19] have derived a correction function to deal with long laser pulses, the purpose of the present paper is not to perform a full simulation of the lidar return signal, but rather to determine the feasibility of retrieving vertical profiles from the derived measurements of column abundance.

A forward model is therefore defined to relate the column abundance to the vertical profile. If the CCD recording interval were infinitesimally short and the flash-lamp pulse were effectively a delta function, the column abundance at range Z would simply be

$$y(Z) = \int_0^Z [N(z)\mathrm{d}z] + \varepsilon(Z), \tag{3}$$

where $\varepsilon(Z)$ is the noise on this measurement. However, to account for the smearing of vertical resolution caused by both the finite CCD recording interval and the finite length of the flash-lamp pulse, an additional scaling function, $f(Z, z)$, is needed. Given an input profile of mixing ratio $\mathbf{x}^{in}$ at n discrete levels of thickness $\mathrm{d}z$, the shape and length $\mathrm{d}t_{pulse}$ of the pulse, and the length of the recording interval $\mathrm{d}t_{ccd}$, measurement y_i is calculated as

$$y_i = \sum_{j=1}^{n} [f_{i,j}\rho_j x_j^{in}\mathrm{d}z] + \varepsilon_i \quad \text{for } i = 1, \ldots, m, \tag{4}$$

where ρ_j is the atmospheric density at level j. Here $f_{i,j}$ is the scaling factor that weights the contribution of x_j^{in} to y_i as the proportion of the flash-lamp signal that passes through altitude z_j of the profile before being backscattered.

The derivation of $f_{i,j}$ is a two-step procedure, illustrated for a square pulse in Fig. 1. Measurement y_i begins at time t_i, at which time the leading edge of the pulse has reached a higher altitude $[z_{max}(t_i)]$ than has the trailing edge $[z_{min}(t_i)]$. Profile points at altitudes z_j below $z_{min}(t_i)$ will all contribute equally to y_i, but the contribution from profile points between $z_{min}(t_i)$ and $z_{max}(t_i)$ is scaled according to the proportion of the flash-lamp pulse that reaches z_j. This can be expressed as follows:

$$f_j(t) = \begin{cases} 1 & \text{if } z_j \le z_{min}(t) \\ \dfrac{\int_0^{T(t)} S(t')\mathrm{d}t'}{\int_0^{dt_{pulse}} S(t')\mathrm{d}t'} & \text{if } z_{min}(t) < z_j < z_{max}(t), \\ 0 & \text{if } z_j \ge z_{max}(t) \end{cases} \tag{5}$$

where $T(t) = 2[z_{max}(t) - z_j]/c$ and $S(t')$ is the flash-lamp signal as a function of time. Backscattered radiation continues to be collected for measurement

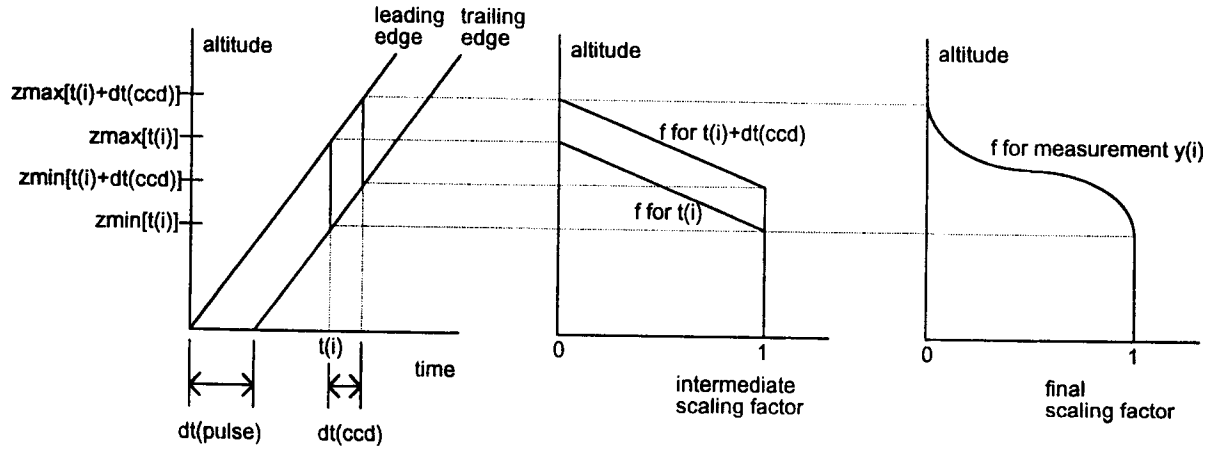

Fig. 1. Schematic view of the vertical propagation of a square flash-lamp pulse of width $\mathrm{d}t_{pulse}$, recorded over interval $\mathrm{d}t_{ccd}$, showing how the forward-model scaling function is derived for a measurement of column abundance.

y_i for the duration of the CCD recording interval, ending at time $t_i + dt_{ccd}$. A series of intermediate scaling factors $f_j(t)$ thus exists for all times between t_i and $t_i + dt_{ccd}$. The final scaling factor relating profile points x_j to measurement y_i is then

$$f_{i,j} = \int_{t_i}^{t_i + dt_{ccd}} f_j(t)dt \qquad (6)$$

normalized to a maximum value of unity. In practice, $f_{i,j}$ is evaluated as the summation of a large number of intermediate scaling factors.

The first simulation of a set of measurements of column abundance was performed for the following conditions. The input profile was set to be a constant mixing ratio of unity. A simple atmospheric density profile, which assumes a surface temperature of 290 K and an adiabatic lapse rate of 10 K/km, was used. The flash-lamp pulse was that shown in Fig. 2, which simulates the rapid rise and slow decay behavior of a xenon-arc lamp. This pulse peaks at 2 μs and decays to 0.01% of the maximum signal after 25.5 μs, with a full-width at half-maximum (FWHM) of approximately 4.9 μs. For a backscattered square pulse, this FWHM would correspond to an uncertainty of 0.73 km in altitude.

The CCD recording interval was set at 5 μs, corresponding to the anticipated illumination of 10 columns of the detector array with a typical charge-transfer time of 0.5 μs per column. For this example, the number of measurements m was 20, giving a maximum altitude of 15 km for the measurements ($z_{top} = 0.5\ mcdt_{ccd}$). The number of profile points n was also set to 20, the maximum possible value, corresponding to a layer thickness of 0.75 km. Random measurement error ε_i was added to each measurement y_i, such that the standard deviation σ_i was equal to 1.0% of y_i. This was chosen based on the signal-to-noise calculations discussed in Section 2, as it can be shown that the signal-to-noise for column abundance is the product of the signal to noise on a spectrum and the optical depth. A signal-to-noise ratio of 1000 (0.1% noise) on the spectrum yields a signal-to-noise ratio of 100 (1% noise) on the column abundance for a typical optical depth of 0.1 and better values of signal to noise for larger optical depths.

For a more accurate calculation of the column abundance, the input profile was linearly interpolated onto a finer altitude grid, with a layer thickness of 0.075 km, and both **f** and **y** were evlauated with this fine grid profile. Figure 3 shows the functions **f** calculated for these conditions. These were used to generate a set of simulated measurements of column abundance as a function of the altitude of the backscattering layer, with the total column increasing with the distance traveled by the flash-lamp pulse.

4. Retrieval of Vertical Profiles

Having generated a set of pseudo measurements of column abundance, the mixing-ratio profile $\hat{\mathbf{x}}$ and its covariance $\hat{\mathbf{S}}$ can be retrieved with the optimal estima-

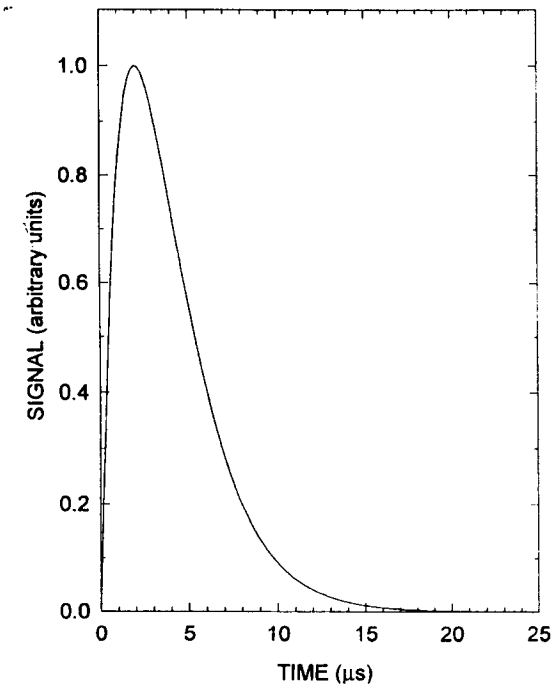

Fig. 2. Time evolution of the simulated flash-lamp pulse, which peaks at 2 μs, has a FWHM of approximately 4.9 μs, and decays to 0.01% of the maximum signal after 25.5 μs.

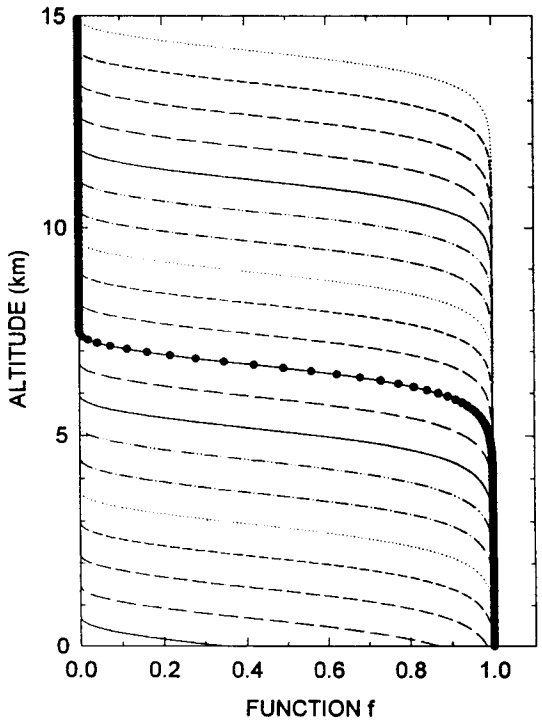

Fig. 3. Forward-model scaling functions (the rows of **f**) calculated for the flash-lamp pulse of Fig. 2 and a CCD recording interval of 5 μs. The solid curve with circles shows the function corresponding to the tenth measurement.

tion equations in the form derived by Rodgers[8]:

$$\hat{\mathbf{x}} = \mathbf{x}_0 + \mathbf{S}_0\mathbf{K}^T(\mathbf{K}\mathbf{S}_0\mathbf{K}^T + \mathbf{S}_y)^{-1}(\mathbf{y} - \mathbf{K}\mathbf{x}_0), \quad (7)$$

$$\hat{\mathbf{S}} = \mathbf{S}_0 - \mathbf{S}_0\mathbf{K}^T(\mathbf{K}\mathbf{S}_0\mathbf{K}^T + \mathbf{S}_y)^{-1}\mathbf{K}\mathbf{S}_0. \quad (8)$$

Here $\mathbf{x}_0$ is the *a priori* estimate of the true profile $\mathbf{x}$ with error covariance $\mathbf{S}_0$ and $\mathbf{K}$ is the weighting-function matrix. These equations combine the virtual measurement obtained from the *a priori* information with the real measurements to give the best estimate of the profile and its covariance. In practice, these equations are solved sequentially, using each scalar measurement y_i in turn to improve the estimate of $\hat{\mathbf{x}}$ from the initial guess through m intermediate values to the final solution.

The weighting-function matrix used in the optimal estimation equations is defined as

$$\mathbf{K} = \frac{\partial F}{\partial \mathbf{x}}, \quad (9)$$

where F is the forward model. Each row of $\mathbf{K}$ is a weighting function, which shows how a given measurement is sensitive to changes in each of the profile values. $\mathbf{K}$ was derived by perturbing each element of $\mathbf{x}^{in}$ in turn and calculating the resulting perturbations in each element of $\mathbf{y}$. Again, for improved accuracy, the interpolated fine grid profile was used in this calculation, with the 10 fine grid points in a layer of $\mathbf{x}^{in}$ being perturbed together in a top-hat arrangement and the perturbed $\mathbf{y}$ being calculated with the perturbed fine grid profile. Figure 4 shows the weighting functions derived from the data above, illustrating the region of the profile that is represented by each measurement and giving a general idea of the information content of the set of measurements. In this case, they are equivalent to the functions $\mathbf{f}$, scaled by the spacing dz of the profile points and by the atmospheric density.

The initial estimate of the profile, $\mathbf{x}_0$, was chosen to be 0 at all 20 levels and was assigned an error covariance $\mathbf{S}_0$ of 1 for all diagonal elements and 0 for all off-diagonal elements, giving the initial guess little weight in the retrieval. The measurement noise covariance $\mathbf{S}_y$ has diagonal elements σ_i^2 and was also assumed to have no interchannel correlation. The vertical profile retrieved with sequential estimation is plotted in Fig. 5, along with two curves showing $\hat{\mathbf{x}} \pm \hat{\sigma}_{\mathbf{x}}$, where $\hat{\sigma}_{\mathbf{x}}^2$ is the retrieved variance. Clearly, the vertical profile is retrievable but has a significant uncertainty; methods of improving the accuracy of the retrieved profile are addressed below.

An alternative method of performing the retrieval is to use a set of orthogonalized weighting functions. It can be shown[8] that the eigenvectors of $\mathbf{K}^T\mathbf{K}$ are the basis vectors $\mathbf{r}_j$ ($j = 1$ to n) identifying that part of the profile space that is represented by the weighting functions. The profile $\mathbf{x}$ can be regarded as a linear combination of these eigenvectors:

$$\mathbf{x} = \sum_{j=1}^{n} a_j\mathbf{r}_j = \mathbf{R}\mathbf{a}, \quad (10)$$

where $\mathbf{r}_j$ are the columns of matrix $\mathbf{R}$ and a_j are the

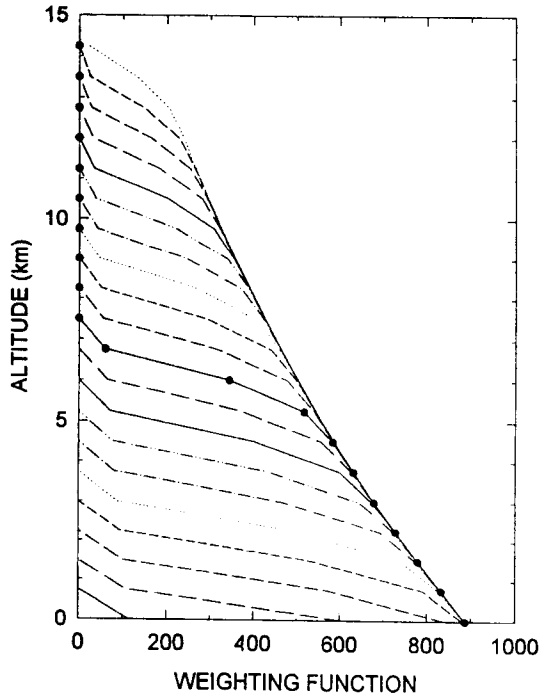

Fig. 4. Weighting functions (the rows of $\mathbf{K}$) calculated for the retrieval described in the text by perturbing $\mathbf{x}^{in}$ and calculating the resulting perturbation in $\mathbf{y}$. The solid curve with circles shows the weighting function corresponding to the tenth measurement.

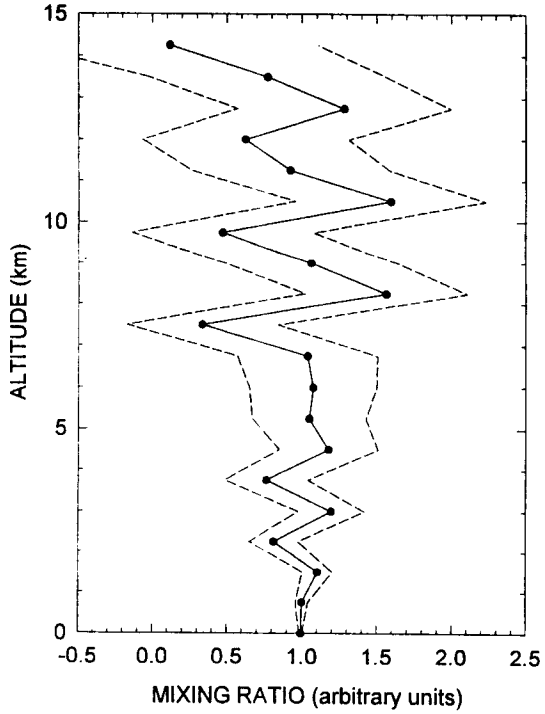

Fig. 5. Vertical profile of the mixing ratio retrieved from the simulated measurements (solid curve with circles), and the uncertainties in this profile defined by $\hat{\mathbf{x}} \pm \hat{\sigma}_{\mathbf{x}}$ (dashed lines), where $\hat{\sigma}_{\mathbf{x}}^2$ is the retrieved variance.

coefficients that determine the relative contribution of each $\mathbf{r}_j$ to $\mathbf{x}$. The eigenvectors of $\mathbf{K}^T\mathbf{K}$ are plotted in Fig. 6, in which they can be seen to represent different frequency scales of the profile, in a similar manner to a Fourier series.

Having derived matrix $\mathbf{R}$, it is possible to calculate the vector of coefficients, $\mathbf{a}^{in}$, that corresponds to $\mathbf{x}^{in}$ and the initial covariance matrix $\mathbf{S}_a = \mathbf{R}^{-1}\mathbf{S}_0(\mathbf{R}^T)^{-1}$. Then, by perturbing $\mathbf{a}^{in}$, and calculating the resulting perturbed $\mathbf{x}^{in}$, and hence the perturbed measurements $\mathbf{y}$, a new weighting-function matrix, $\partial F/\partial_{\mathbf{a}}$, can be generated and used in the optimal estimation equations to retrieve $\hat{\mathbf{a}}$, and hence $\hat{\mathbf{x}}$. With this method, the number of coefficients to be retrieved can be varied from 1 to n, allowing frequency components that are known to be negligible in the profile to be omitted from the retrieval. Figure 7 shows the profiles of mixing ratio retrieved by the use of this method for an increasing number of retrieved coefficients, clearly showing how the profile is built up as a linear combination of the eigenvectors in Fig. 6. The final profile in this series, retrieved with all 20 coefficients, is similar to that in Fig. 5; however, it is not identical because the perturbation of $\mathbf{x}^{in}$ by the two methods was very different.

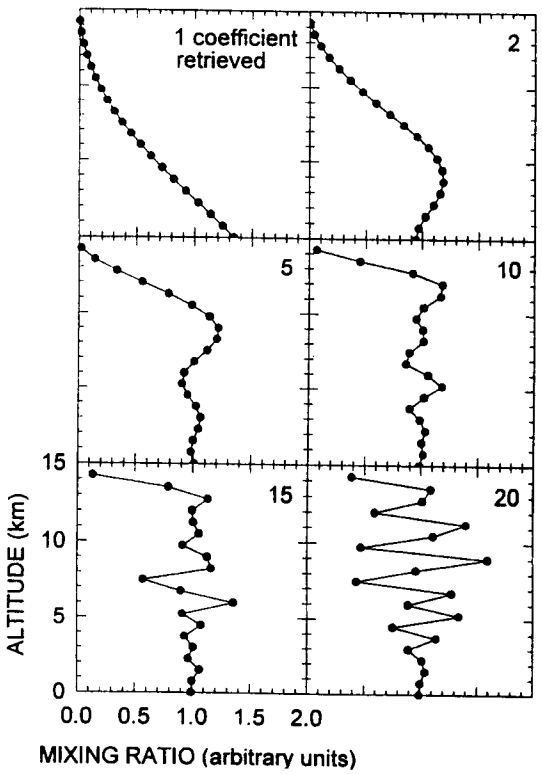

Fig. 7. Vertical profile of the mixing ratio retrieved with the eigenvector method with 1, 2, 5, 10, 15, and 20 coefficients retrieved, as indicated.

5. Vertical Resolution of the Retrieved Profiles

For the purposes of characterizing the retrieval system, two additional sets of functions can be calculated: contribution functions and averaging kernels. The matrix of contribution functions is defined as

$$\mathbf{D} = \frac{\partial I}{\partial \mathbf{y}}, \tag{11}$$

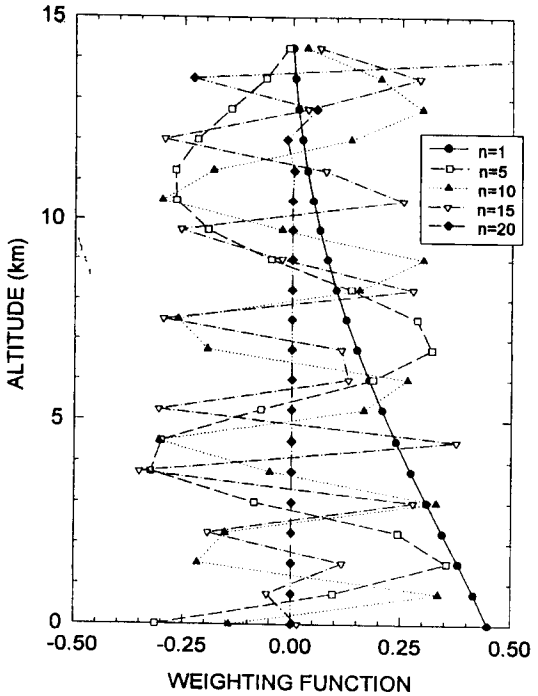

Fig. 6. Eigenvectors of $\mathbf{K}^T\mathbf{K}$ for the retrieval described in the text. For clarity, only five are plotted.

where $I(\mathbf{y}, \mathbf{b}, \mathbf{c})$ is the inverse model that defines the retrieved profile $\hat{\mathbf{x}}$ as a function of $\mathbf{y}$, with $\mathbf{c}$ being a vector of parameters that are used in the retrieval but not in the forward model. Each column of $\mathbf{D}$ represents the contribution to the solution that is due to a unit change in the corresponding element of $\mathbf{y}$. $\mathbf{D}$ can be calculated with the matrix equation[8]

$$\mathbf{D} = \mathbf{S}_0\mathbf{K}^T(\mathbf{K}\mathbf{S}_0\mathbf{K}^T + \mathbf{S}_y)^{-1}. \tag{12}$$

The contribution functions derived for the retrieval of Fig. 5 are shown in Fig. 8. These functions indicate the complexity of the way in which each measurement contributes to the final profile, illustrating how an error in y_i will lead to a compensating series of errors in $\hat{\mathbf{x}}$.

The matrix of averaging kernels is defined as

$$\mathbf{A} = \frac{\partial T}{\partial \mathbf{x}}, \tag{13}$$

where $T = I(F)$ is the transfer function relating the retrieved profile to the real profile. $\mathbf{A}$ can be calculated simply as the product of $\mathbf{D}$ and $\mathbf{K}$. The value of the retrieved profile at a given altitude is equal to the average of the real profile weighted by the corresponding row of $\mathbf{A}$. The averating kernels calculated for the above retrieval are plotted in Fig. 9. The width of the primary peak of each of these curves is a

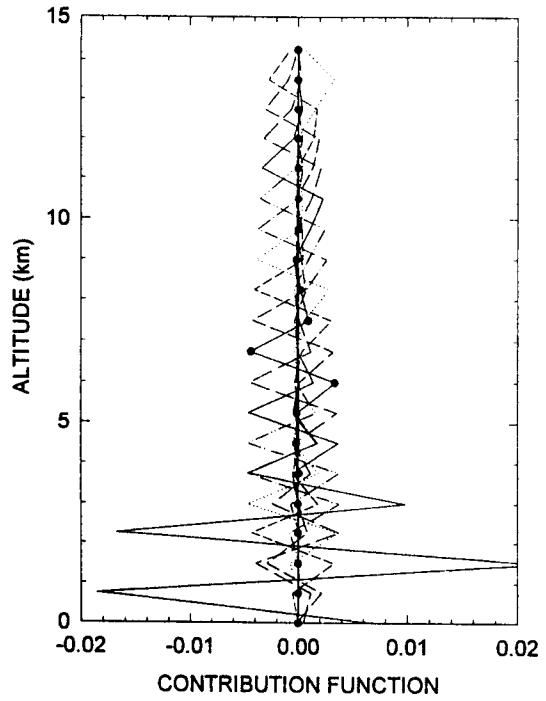

Fig. 8. Contribution functions (the columns of **D**) calculated for the retrieval of Fig. 5. The solid curve with circles shows the contribution function corresponding to the tenth profile point.

qualitative measure of the resolution of the retrieval system. Figure 9 shows that there is a gradual decrease in resolution with altitude, with the FWHM increasing from approximately 0.75 to 1.5 km over the range of the profile. This is due to the increase in measurement noise with altitude. The incomplete averaging kernels at the highest altitudes, and hence the poorer retrievals above 12 km in Fig. 5, are because the measurements have been limited to an altitude of 15 km. More accurate retrievals could be obtained above 12 km if measurements corresponding to altitudes above 15 km were included in the retrieval.

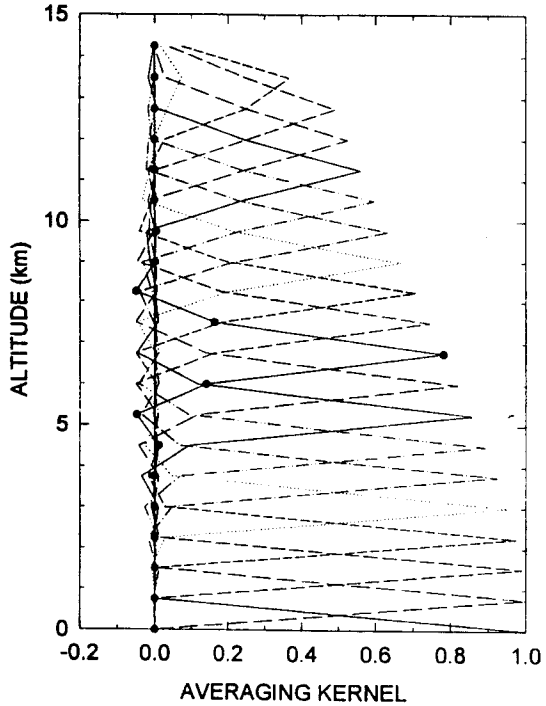

Fig. 9. Averaging kernels (the rows of **A**) calculated for the retrieval of Fig. 5. The solid curve with circles shows the averaging kernel corresponding to the tenth retrieved profile point.

A more quantitative measure of the vertical resolution is the width of the averaging kernels as defined by the Backus–Gilbert spread[15,20]:

$$s(z) = \frac{12}{a(z)^2} \int_0^{z_{top}} (z - z')^2 A(z, z')^2 dz', \qquad (14)$$

where $a(z)$ is the area of the averaging kernel for height z, required if $A(z)$ is not normalized, and the factor 12 makes the spread equal to the width for a boxcar averaging kernel. This integration is approximated by linearly interpolating each row of **A** onto a finer grid (again 10 points per 0.75-km layer) and calculating the spread by the use of these interpolated averaging kernels. As shown by the curve labeled $n = 20$ in Fig. 12, below, the spread for the simulated retrieval discussed above lies between 0.6 and 1.4 km and increases with altitude, consistent with the gradual broadening of the averaging kernels with altitude, as shown in Fig. 9.

This spread is partly determined by the number and spacing of the retrieved profile points, which, in Rodgers' method, must be chosen before performing the retrieval. However, in general, the retrieval of a vertical profile can be optimized to minimize either this spread or the retrieved noise, or some linear combination of the two. The technique for relating the vertical resolution of the retrieved profile to its sensitivity to random noise on the measurements was developed by Backus and Gilbert[20] for remote sounding of the structure of the solid Earth and was subsequently applied to atmospheric remote sounding by Conrath.[21]

Following the formulation outlined by Conrathy,[21] the change in measurement y_i caused by a change Δx in the atmospheric profile at altitude z is

$$\Delta y_i = \int_0^{\infty} K_i(z) \Delta x(z) dz, \qquad (15)$$

where $K_i(z)$ is the weighting function for the ith measurement. The change in the retrieved profile can be expressed as a linear combination of Δy_i:

$$\Delta \hat{x}(z) = \sum_{i=1}^{m} b_i(z) \Delta y_i \qquad (16)$$

where the coefficients $b_i(z)$ depend on the method of

inversion. Substitution of Eq. (15) into Eq. (16) gives

$$\Delta\hat{x}(z) = \int_0^\infty \left[\sum_{i=1}^{m} b_i(z)K_i(z')\right]\Delta x(z')\mathrm{d}z'$$

$$= \int_0^\infty A(z, z')\Delta x(z')\mathrm{d}z', \qquad (17)$$

where $A(z, z')$ is again the averaging kernel.

It is the choice of the coefficients $b_i(z)$ that determines how the measurements are weighted to obtain the profile, and hence how a linear combination of the vertical resolution and the noise on the retrieved profile is minimized. This is achieved as follows. The vertical resolution is represented by the spread [Eq. (14)], and the noise is defined by the variance on the retrieved profile

$$\hat{\sigma}_x^2(z) = \mathbf{b}^T(z)\mathbf{S}_y\mathbf{b}(z), \qquad (18)$$

where $\mathbf{b}(z)$ is a vector of the inversion coefficients and $\mathbf{S}_y$ is the measurement-error covariance matrix. A linear combination of the spread and the retrieved variance is given by

$$Q(z) = qs(z) + (1 - q)r\hat{\sigma}_x^2(z). \qquad (19)$$

The parameter r is simply a scaling factor that gives both terms the same physical dimensions, and the parameter q determines the relative minimization of the spread and the variance. By varying the value of q between 0 and 1, one can construct a trade-off curve of vertical resolution versus accuracy. Conrath[21] outlines the additional steps required to calculate the inversion coefficients for a given value of q at a given altitude z, which then allows the curves of $s(z; q)$ versus $\hat{\sigma}_x(z; q)$ to be generated. It is also possible to use these coefficients to perform a retrieval, but in practice the method of sequential estimation is preferred for this purpose; the trade-off curves are most useful for demonstrating the intrinsic vertical resolution of a system and for choosing the vertical spacing to be used in the retrieval that will give an acceptable level of noise.

Trade-off curves were thus calculated for each altitude of the retrieved profile in the simulation described above by the use of the previously defined matrices $\mathbf{K}$ and $\mathbf{S}_y$. The results are plotted for selected altitudes in Fig. 10. These trade-off curves are encouraging, as they show that reasonable accuracy can be achieved with good vertical resolution. If, for example, the error is 0.1 in mixing ratio (equivalent to 10% for the profile under consideration), the resolution of the retrieved profile will be less than 1 km near the ground and will increase with altitude to 2.5 km resolution at 12.0 km altitude and to 5 km at 12.75 km. If an error of 0.2 (equivalent to 20%) is acceptable, the vertical resolution will be less than 2 km for all levels up to 12.75 km. The degradation in resolution with altitude is due to the broadening of the averaging kernels, and the poorer resolution for the two highest layers is due to the truncation of the weighting function above 15 km.

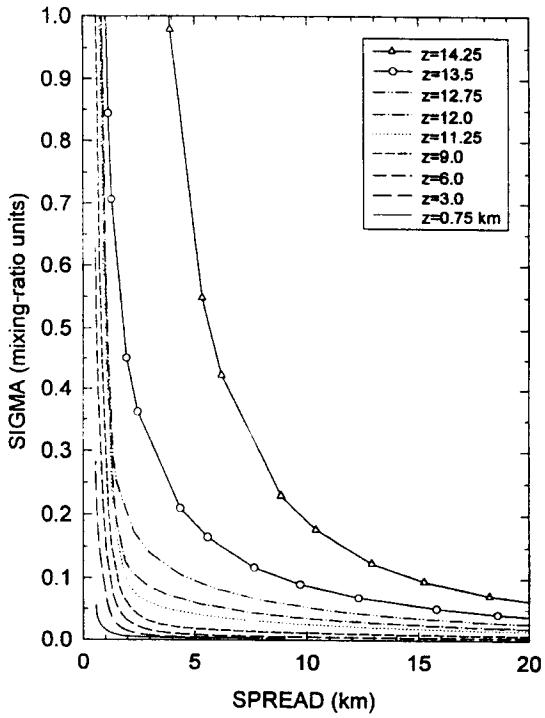

Fig. 10. Backus–Gilbert trade-off curves of spread versus the standard deviation of $\hat{\mathbf{x}}$ as a result of random measurement errors given by $\mathbf{S}_y$, calculated for each level of the retrieved profile. For clarity, some of the curves below 11.25 km have been omitted from this plot.

These trade-off curves clearly show that performing the retrieval on a grid with a vertical spacing of 0.75 km, and thereby forcing the measurements to give a spread close to 1.0 km, will result in large errors in the retrieved profile, as was the case for the retrieval shown in Fig. 5. To reduce these errors, the retrieval was repeated with a coarser grid spacing, corresponding to a poorer vertical resolution. The profiles retrieved by the use of 10 points at 1.5-km intervals and 5 points at 3-km intervals are compared in Fig. 11. As expected, the curves of $\hat{\mathbf{x}} \pm \hat{\sigma}_\mathbf{x}$ show a significant improvement in error, at the expense of the vertical resolution. This is confirmed by Figs. 12 and 13. In the former, the spread can be seen to increase to approximately 1.2 and 2.4 km, respectively, for the retrievals of 10 and 5 profile points. Similarly, although not plotted, the FWHM's of the peaks of the averaging kernels also increase to approximately 1.5 and 3 km for these two cases. Conversely, in Fig. 13, the error on the profile can be seen to decrease as fewer points are retrieved, being less than 0.1 for $n = 5$. From these results, it can be concluded that the ranging instrument will be capable of reasonable accuracy (σ less than 30%) at moderate vertical resolution (spread less than 3 km), with some flexibility in the choice of which parameter to optimize in the retrieval process.

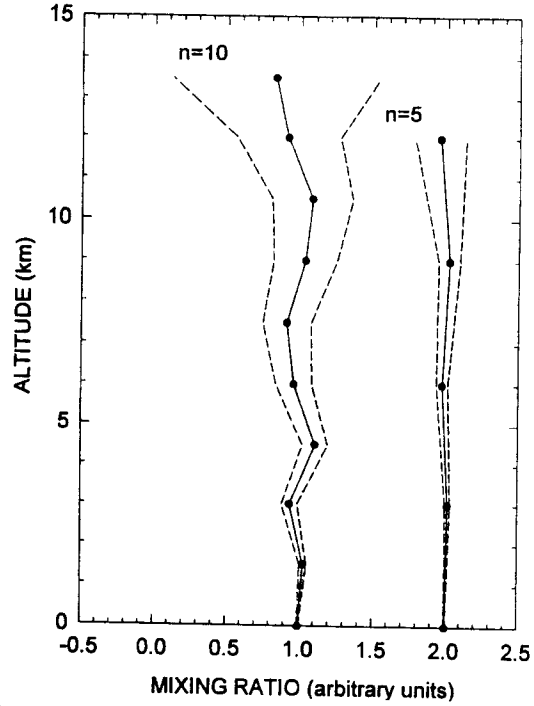

Fig. 11. Vertical profile of the mixing ratio (solid curve with circles) and $\hat{\mathbf{x}} \pm \hat{\sigma}_{\mathbf{x}}$ (dashed curves) retrieved when the number of profile points is limited to 10 and 5 for a set of 20 measurements. For clarity, the profiles for $n = 5$ have been offset by 2 mixing-ratio units.

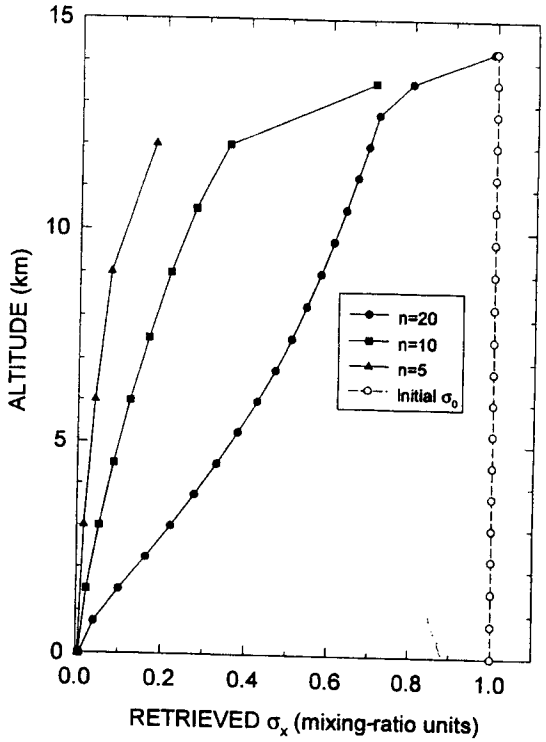

Fig. 13. Standard deviation on the profile retrieved at 20, 10, and 5 points with the set of 20 measurements discussed in the text. The standard deviation on the initial guess for the 20-point retrieval is included; it has the same value at fewer points for the 10- and 5-point retrievals.

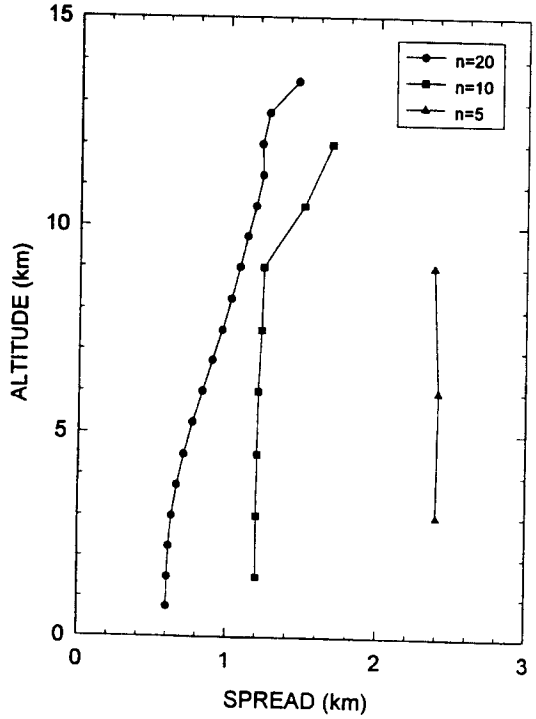

Fig. 12. Backus–Gilbert spread for the retrieval of 20, 10, and 5 profile points with the set of 20 measurements discussed in the text. The first and last points have been omitted from the plot because the incomplete averaging kernels for these points distort the value of the spread.

6. Additional Retrievals with Different Input Parameters

For comparison with the retrieval of Fig. 5, a series of additional retrievals were performed to investigate how the input parameters of measurement error, flash-lamp pulse length, CCD recording interval, and mixing-ratio profile each affect the accuracy and the vertical resolution of the retrieved profile. In all cases an initial estimate of 0 was used for $\mathbf{x}_0$, with $\mathbf{S}_0$ equal to the unit matrix. Unless otherwise stated, the input parameters were the same as those for the initial example, given in Section 3: the flash-lamp pulse was that of Fig. 2; the input profile was constant, with 20 profile points and a layer thickness of 0.75 km; the CCD recording interval was 5 μs; and the number of measurements was 20.

The first parameter to be investigated was the measurement error. Backus–Gilbert trade-off curves were calculated and retrievals were performed for two cases: a reduction in the measurement error by a factor of 10, such that the standard deviation σ_i was equal to 0.1% of measurement y_i, and an increase by a factor of 5, such that σ_i was equal to 5.0% of y_i. A change in $\mathbf{S}_y$ leads directly to a change in the error on the retrieved profile, as can be seen in Eqs. (8) and (18). The effect on the trade-off curves is shown in Fig. 14, in which the curves for measurement errors of 0.1%, 1.0%, and 5.0% at the intermediate altitude of 9 km are compared. Similar results are obtained

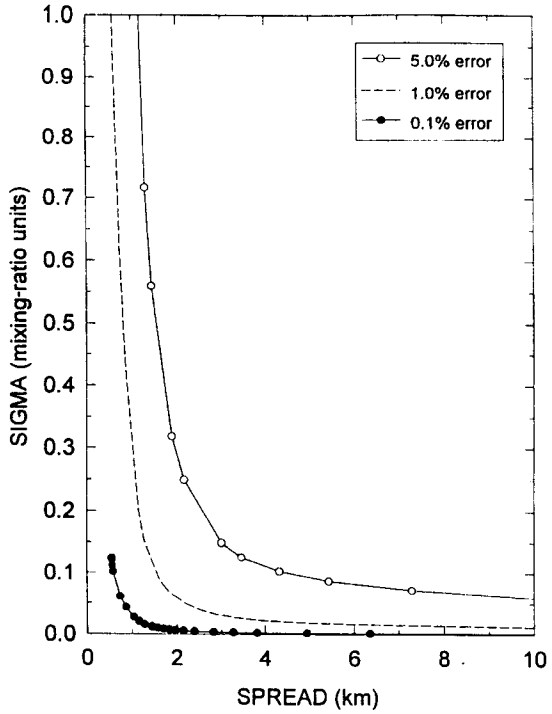

Fig. 14. Backus–Gilbert trade-off curves of spread versus the standard deviation of $\hat{\mathbf{x}}$ for the 9-km layer, calculated for measurement error σ_i equal to 5.0%, 1.0% and 0.1% of measurement y_i.

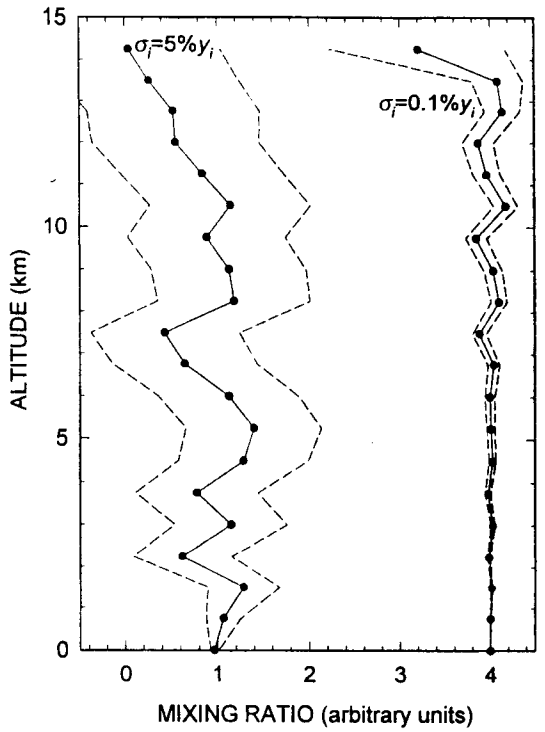

Fig. 15. Vertical profile of the mixing ratio (solid curve with circles) and $\hat{\mathbf{x}} \pm \hat{\sigma}_{\mathbf{x}}$ (dashed curves) retrieved for measurement error σ_i equal to 5.0% and 0.1% of measurement y_i. For clarity, the profiles for 0.1% error have been offset by 3 mixing-ratio units.

at other altitudes. As expected, these results demonstrate that the smaller the measurement error, the smaller the error (or the better the vertical resolution) that can be achieved for the retrieved profile. For the 9-km layer, if an error of 0.1 in mixing ratio is desired, the resolution of the retrieved profile will be less than 0.6 km, 1.5 km, and 4.5 km, respectively, for measurement errors of 0.1%, 1.0%, and 5.0%. Conversely, if the profile is retrieved on a grid with a vertical spacing of 0.75 km, i.e., that used in Fig. 5, the profile errors will be large but will decrease with decreasing measurement error, as illustrated by the retrievals in Fig. 15. Clearly, to optimize the retrieval of vertical profiles with the ranging instrument, the signal to noise of the measurements should be maximized; in practice, it should be possible to improve this signal to noise by integrating a series of pulses of the flash lamp on the CCD before readout.

The next input parameter to be studied was the flash-lamp pulse. Trade-off curves were calculated for three additional pulses, peaking at 0.5, 4, and 8 μs (compared with 2 μs for the pulse in Fig. 2) and with total pulse energy correspondingly scaled by one-quarter, two, and four times that of the pulse in Fig. 2. The FWHM's of these four pulses are 1.2, 4.9, 9.8, and 19.6 μs, which correspond to uncertainties of 0.18, 0.73, 1.5, and 2.9 km in altitude, respectively. The trade-off curves for all four pulses at 9 km are compared in Fig. 16, from which two conclusions can be drawn. First, decreasing the pulse width below a FWHM of 4.9 μs has little effect, which follows from the fact that the uncertainty in altitude of 0.73 km that is associated with this FWHM is almost the same as the 0.75-km grid spacing of the profile. Second, increasing the pulse width above a FWHM of 4.9 μs does influence the trade-off curves, causing either poorer vertical resolution or large errors on the

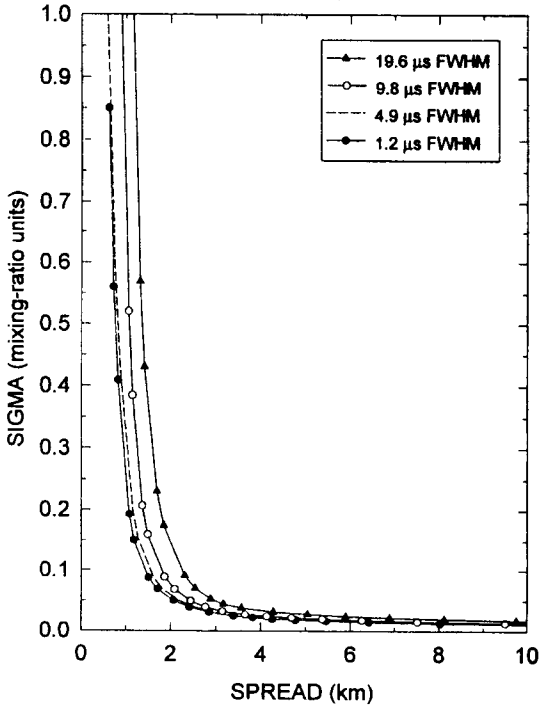

Fig. 16. Backus–Gilbert trade-off curves of spread versus the standard deviation of $\hat{\mathbf{x}}$ for the 9-km layer, calculated for the four flash-lamp pulses discussed in the text.

retrieved profile. Increasing the pulse width increases the extent of the region through which the signal partially passes, thereby smearing out the forward-model scaling functions over a larger altitude range (see Fig. 1) and hence smearing out the weighting functions. The resulting averaging kernels are broader, and the vertical resolution is therefore worse. Thus the optimum flash-lamp pulse for the ranging instrument will have an equivalent width in altitude equal to or less than the grid spacing of the profile, as there is little advantage to having a smaller width and a degradation in performance if the width is larger.

The third parameter to be varied was the CCD recording interval. For comparison with the baseline case of 5 μs, retrievals were performed for both a shorter interval of 2 μs and a longer interval of 10 μs. These correspond to the illumination of 4 and 50 columns, respectively, of a CCD array having a typical charge-transfer time of 0.5 μs per column. Decreasing the recording interval has two effects: it reduces the region of partial transmission of the pulse (see Fig. 1 again) and it increases the number of measurements, $m = 2z_{top}/cdt_{ccd}$, so that more profile points can be retrieved at higher vertical resolution for a given maximum altitude. Trade-off curves and retrievals were therefore calculated for both the maximum possible number of profile points $n = m$, giving 50, 20, and 10 points for the intervals of 2, 5, and 10 μs, and also for $n = 10$ for the 2- and 5-μs intervals. To illustrate how dt_{ccd} and the value of n influence the retrieved profiles, the resulting spreads are presented in Fig. 17, and the errors on the retrieval are presented in Fig. 18. These results indicate that making $n = m$ for a given recording interval forces higher vertical resolution for smaller dt_{ccd}, thus making the error larger and the spread smaller as dt_{ccd} decreases. Making $n = m$ is equivalent to minimizing the spread and maximizing the noise on the grade-off curves. (However, for $n = 50$, this minimum spread is also limited by the width of the flash-lamp pulse, which gives an FWHM uncertainty of 0.73 km in altitude in this example; when this is reduced to make dt_{ccd} the controlling factor, the spread for $n = 50$ becomes a smooth curve varing from 0.25 km at the ground to 0.6 at 14 km.) In contrast, if n is limited to 10 points while m is unchanged, the averaging kernels, and hence the spreads, are forced to become similar for all three values of dt_{ccd}. The retrieved error then decreases as dt_{ccd} decreases, as there are more measurements to constrain the retrieval of a fixed number of points. From these results, the optimum CCD recording interval will be as short as possible to improve the vertical resolution by reducing the slope of the forward-model scaling functions and to maximize the number of measurements, and fewer profile points will be retrieved than there are measurements, giving better constraints on the retrieval.

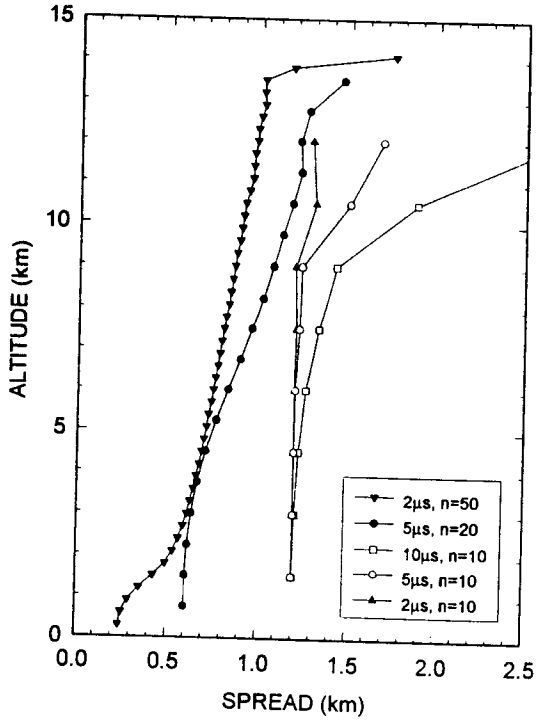

Fig. 17. Backus–Gilbert spread for the retrieval of 10 and 50 points for a CCD recording interval of 2 μs, 10 and 20 points for an interval of 5 μs, and 10 points for an interval of 10 μs. The first and last points have been omitted from the plot because the incomplete averaging kernels for these points distort the value of the spread.

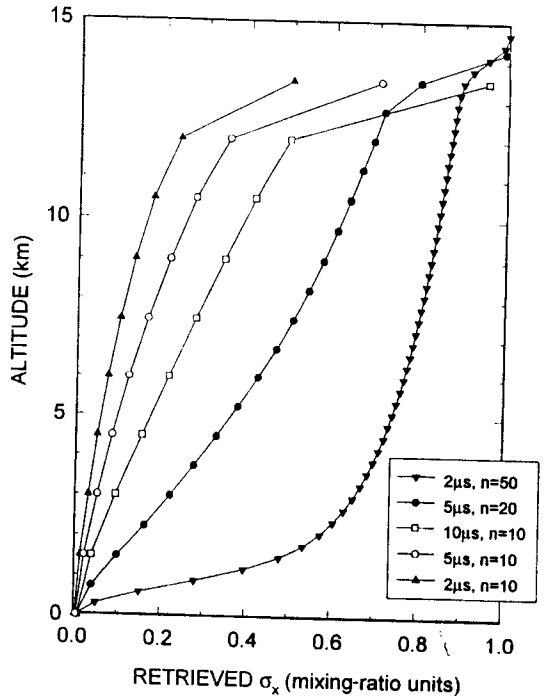

Fig. 18. Standard deviation on the profile retrieved at 10 and 50 points for a CCD recording interval of 2 μs, 10 and 20 points for an interval of 5 μs, and 10 points for an interval of 10 μs.

The last set of retrievals was performed for different mixing-ratio profiles. In Fig. 19, an input profile of a Gaussian layer centered at 7.5 km with a FWHM of 4.7 km ($\sigma = 2.0$ km) was used, with all other parameters identical to those for the retrieval of Fig. 5. Both the input profile and the retrieved profile for

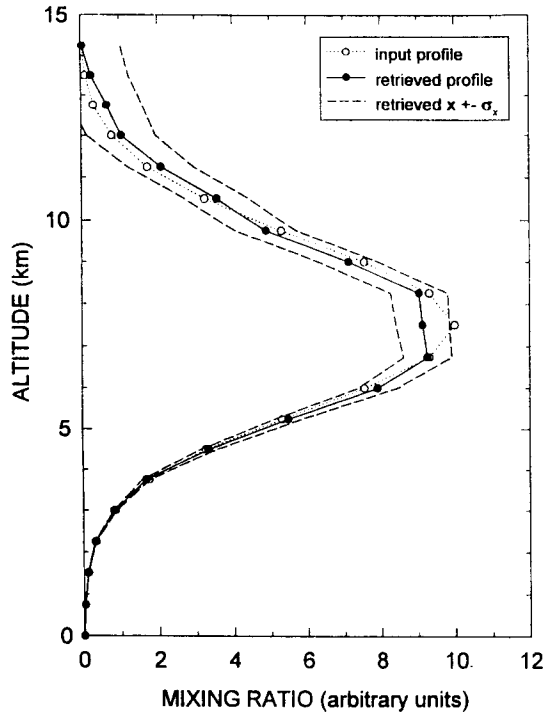

Fig. 19. Input Gaussian profile of the mixing ratio, along with the corresponding retrieved profile and $\hat{\mathbf{x}} \pm \hat{\sigma}$.

the maximum number of profile points, $n = m = 20$, are shown. At this point spacing, the averaging kernels are similar to those for the constant mixing ratio below 7.5 km, giving a spread of approximately 0.6 km, but broaden above this altitude, leading to an increase in the spread with altitude to approximately 3-km resolution at 13 km. The error on the retrieved profile also increases significantly with altitude above the peak of the profile, because the measured column abundances, and hence the measurement errors, become quite large when they include the peak values of the mixing ratio. However, the good agreement between the input and retrieved profiles in Fig. 19 demonstrates that it should be possible to use the ranging instrument to retrieve more complex atmospheric structures than just the simple profile of constant mixing ratio.

7. Conclusions

In this paper, the principles of retrieval theory have been used to model the performance of a recently conceived ranging instrument that combines the advantages of UV–visible absorption spectroscopy with those of lidar profiling. The use of a broadband source and a two-dimensional CCD array detector allows individual spectra to be measured at a series of discrete time intervals, from which column abundances can be simultaneously derived for different atmospheric constitutents. This modeling study has demonstrated the feasibility of using the ranging instrument to retrieve vertical profiles of these constituents in the troposphere and lower stratosphere. Retrievals of both constant and structured mixing-ratio profiles have been performed, the latter demonstrating that it should be possible to resolve vertical structure in the atmosphere with the ranging instrument.

Backus–Gilbert curves have been used to demonstrate the trade-off between minimizing the vertical resolution and minimizing the error on the retrieved profile for a series of different input parameters. Retrieving fewer profile points improves the error at the expense of coarser vertical resolution. Depending on whether accuracy or resolution is optimized in the retrieval, it should be possible to retrieve profiles with the ranging instrument at accuracies better than 30% and resolution better than 3 km up to altitudes of 12–15 km.

Various factors influencing the quality of the retrievals that will be achievable with the ranging instrument have also been investigated. First, the noise on the measurements significantly affects the quality, with larger measurement noise limiting the accuracy and vertical resolution that can be obtained. This suggests that a large number of measurements should be integrated on the CCD to improve the signal to noise as much as possible. Second, the duration of the flash-lamp pulse also affects the trade-off curves, as it determines the region through which the pulse is partially transmitted and therefore the slope of the weighting functions. The optimum pulse will have a FWHM (in altitude) equal to or less than the grid spacing of the profile, as there is a degradation in performance for larger widths and little advantage to a smaller width. Third, the length of the CCD recording interval defines the number of measurements and therefore the maximum number of profile points that can be retrieved and also contributes to the region of partial transmission of the flash-lamp pulse. The optimum CCD recording interval will be as short as possible to reduce the slope of the weighting functions and to maximize the number of measurements, and fewer profile points will be retrieved than there are measurements, giving better constraints on the retrieval.

References

1. J. F. Noxon, "Nitrogen dioxide in the stratosphere and troposphere measured by ground-based absorption spectroscopy," Science **189,** 547–549 (1975).
2. R. M. Schotland, "Some observations of the vertical profile of water vapor by means of a laser optical radar," in *Proceedings of the Fourth Symposium on Remote Sensing of Environment* (University of Michigan, Ann Arbor, Michigan, 1966), pp. 273–277.
3. J. Pelon and G. Mégie, "Ozone monitoring in the troposphere and lower stratosphere: evaluation and operation of a ground-based lidar station," J. Geophys. Res. **87,** 4947–4955 (1982).
4. R. L. Jones, "A novel ranging UV–visible spectrometer for remote sensing of the troposphere," in *Optical Methods in Atmospheric Chemistry,* U. Platt and H. I. Schiff, eds. Proc. Soc. Photo-Opt. Instrum. Eng. **1715,** 393–402 (1992).
5. R. L. McKenzie, P. V. Johnston, C. T. McElroy, J. B. Kerr, and S. Solomon, "Altitude distributions of stratospheric constituents from ground-based measurements at twilight," J. Geophys. Res. **96,** 15499–15512 (1991).
6. K. E. Preston and R. L. Jones, "Vertical profiling of NO_2 based

on twilight zenith sky grond-based measurements," Eos **75**(16) Supplement, 96 (1994).
7. S. Twomey, *Introduction to the Mathematics of Inversion in Remote Sensing and Indirect Measurements* (Elsevier, Amsterdam, 1977).
8. C. D. Rodgers, "Retrieval of atmospheric temperature and composition from remote measurements of thermal radiation," Rev. Geophys. Space Phys. **14**, 609–624 (1976).
9. E. R. Westwater and O. N. Strand, "Inversion techniques," in *Remote Sensing of the Troposphere*, V. E. Derr, ed. (U.S. Dept. of Commerce, Washington, D.C., 1972), pp. 16.1–16.13.
10. S. Twomey, "On the numerical solution of Fredholm integral equations of the first kind by the inversion of the linear system produced by quadrature," J. Assoc. Comput. Mach. **10**, 97–101 (1963).
11. A. N. Tikhonov, "Solution of incorrectly formulated problems and the regularization method," Sov. Math. **4**, 1035–1038 (1963).
12. B. P. Ivanenko and I. E. Naats, "Integral-equation method for interpreting laser-sounding data on atmospheric gas components using differential absorption," Opt. Lett. **6**, 305–307 (1981).
13. R. E. Warren, "Detection and discrimination using multiple-wavelength differential absorption lidar," Appl. Opt. **24**, 3541–3545 (1985).
14. R. E. Warren, "Adaptive Kalman–Bucy filter for differential absorption lidar time series data," Appl. Opt. **26**, 4755–4760 (1987).
15. C. D. Rodgers, "Characterization and error analysis of profiles retrieved from remote sounding measurements," J. Geophys. Res. **95**, 5587–5595 (1990).
16. J. A. Sunesson, A. Apituley, and D. P. J. Swart, "Differential absorption lidar system for routine monitoring of tropospheric ozone," Appl. Opt. **33**, 7045–7058 (1994).
17. Y. Zhao, T. K. Lea, and R. M. Schotland, "Correction function for the lidar equation and some techniques for incoherent CO_2 lidar data reduction," Appl. Opt. **27**, 2730–2740 (1988).
18. D. J. Fish, R. L. Jones, R. A. Freshwater, H. K. Roscoe, D. J. Oldham, and J. E. Harries, "Total ozone measured during EASOE by a UV–visible spectrometer which observes stars," Geophys. Res. Lett. **21**, 1387–1390 (1994).
19. Y. Zhao and R. M. Hardesty, "Technique for correcting effects of long CO_2 laser pulses in aerosol-backscattered coherent lidar returns," Appl. Opt. **27**, 2719–2729 (1988).
20. G. E. Backus and J. F. Gilbert, "Uniqueness in the inversion of inaccurate gross earth data," Phil. Trans. R. Soc. London Ser. A **266**, 123–192 (1970).
21. B. J. Conrath, "Vertical resolution of temperature profiles obtained from remote radiation measurements," J. Atmos. Sci. **29**, 1262–1271 (1972).